

Banner appropriate to article type will appear here in typeset article

# Effect of rotation on turbulent mixing driven by the Faraday instability.

Narinder Singh<sup>1</sup> and Anikesh Pal<sup>1</sup>†

<sup>1</sup>Department of Mechanical Engineering, Indian Institute of Technology Kanpur, Kanpur 208016, U.P., India

(Received xx; revised xx; accepted xx)

The effect of the rotation on the turbulent mixing of two miscible fluids of small contrasting density, produced by Faraday instability, is investigated using direct numerical simulations (DNS). We demonstrate that at lower forcing amplitudes, the turbulent kinetic energy (*t.k.e.*) increases with an increase in the Coriolis frequency  $f$  till  $(f/\omega)^2 < 0.25$ , where  $\omega$  is the forcing frequency, during the sub-harmonic instability phase. The increase in *t.k.e.* increases the buoyancy flux ( $B_V$ ), which increases the total potential energy (TPE). A portion of TPE is the available potential energy (APE). Some parts of APE can convert to *t.k.e.* via  $B_V$ , whereas the rest converts to internal energy, increasing background potential energy (BPE) through  $\phi_i$ . The remaining TPE also converts to BPE through the diapycnal flux  $\phi_d$  resulting in irreversible mixing. With the saturation of the instability, irreversible mixing ceases. When  $(f/\omega)^2 > 0.25$ , the Coriolis force significantly delays the onset of the sub-harmonic instabilities. During this period, the initial concentration profile diffuses to increase TPE, which eventually expends in BPE. The strong rotational effects suppress *t.k.e.*. Therefore,  $B_V$  and APE become small, and the bulk of the TPE expends to BPE. Since the instability never saturates for  $(f/\omega)^2 > 0.25$ , the  $B_V$  remains non-zero, resulting in a continuous increase in TPE. Conversion of TPE to BPE via  $\phi_d$  continues, and we find prolonged irreversible mixing. At higher forcing amplitudes, the stabilizing effect of rotation is negligible, and the turbulence is less intense and short-lived. Therefore, the irreversible mixing phenomenon also ends quickly for  $(f/\omega)^2 < 0.25$ . However, when  $(f/\omega)^2 > 0.25$  a continuous mixing is observed. We find that the turbulent mixing is efficient at lower forcing amplitudes and rotation rates of  $(f/\omega)^2 > 0.25$ .

**Key words:**

## 1. Introduction

The Faraday instability (Faraday 1831) describes the generation of standing wave patterns at the interface of two immiscible fluids subjected to vertical periodic vibration. However, in a stably stratified two-layer miscible fluid system, these standing waves become highly

† Email address for correspondence: pala@iitk.ac.in

**Abstract must not spill onto p.2**

disorganized above a certain forcing amplitude and start to interact with each other resulting in the mixing of fluids (Zoueshtiagh *et al.* 2009; Amiroudine *et al.* 2012; Diwakar *et al.* 2015). Gréa & Adou (2018); Briard *et al.* (2019) studied the onset and saturation of turbulent mixing owing to Faraday instability in fluids of small contrasting density for a wide range of parameters using theoretical models and DNS. Further experiments were carried out by Briard *et al.* (2020); Cavalier *et al.* (2022) using fresh and salty water to explore the dynamics of turbulent mixing. They found that when the instability is triggered, a natural wavelength appears at the interface between the two fluids. With the increase in amplitude, well-defined structures form that break to produce turbulent mixing. However, owing to the saturation of the instability, the turbulent mixing cannot be sustained for long. Recently, Singh & Pal (2022) presented a theoretical analysis of Faraday instability in miscible fluids under the effect of rotation and corroborated their findings with DNS. They reported that rotational effects stabilize the flow and delay the onset of the sub-harmonic instability at lower forcing amplitudes ( $F$ ), whereas, with an increase in  $F$ , the stabilizing effect of rotation diminishes. They concluded that the instability saturates for  $(f/\omega)^2 < 0.25$ , and the mixing zone size asymptotes. However, for  $(f/\omega)^2 \geq 0.25$ , the instability does not saturate, and the mixing zone size continues to grow. The present investigation aims to quantify the turbulent mixing driven by Faraday instability in terms of the exchanges among the total potential energy (TPE), the background potential energy (BPE), and the available potential energy (APE) under the influence of rotation.

## 2. Problem formulation and numerical details

The two-layer miscible fluid system with small density contrast is considered here, which is driven by vertical periodic oscillations of acceleration  $g(t) = g_0(1 + F \cos(\omega t))$ , where  $g_0$  is the mean acceleration. We consider the density of the mixture to be a linearly varying function of mass concentration such that the lighter fluid with concentration  $C(\rho_2) = 0$  is placed above the denser fluid with  $C(\rho_1) = 1$  in a rectangular domain. The governing equations are the three-dimensional incompressible unsteady Navier–Stokes equations with Boussinesq approximation and are solved in a Cartesian coordinate system on a staggered grid arrangement as discussed in Singh & Pal (2022). We consider periodic boundary conditions for all variables in the  $x_1$  and  $x_2$  (horizontal) directions, whereas at the top and bottom walls ( $x_3$ ), no-slip boundary conditions for velocity vector  $\mathbf{U}$  and Neumann boundary conditions for  $C$  and pressure  $P$  are used. The mixing zone size- $L$  is computed from mean concentration profile  $\langle C \rangle$  (Andrews & Spalding 1990) as  $L = 6 \int_{-\infty}^{+\infty} \langle C \rangle(x_3, t) (1 - \langle C \rangle(x_3, t)) dx_3$ , where  $\langle \cdot \rangle$  denotes the horizontal average. The Brunt Väisälä frequency is defined as  $N = (-2\mathcal{A}g_0\partial\langle C \rangle/\partial x_3)^{1/2}$ , where  $\partial\langle C \rangle/\partial x_3 = -1/L$ . Table 1 shows the key parameters for all simulation cases. We select three cases at each  $F$  depending on the value of  $f/\omega$ , where sub-harmonic instability saturates for  $f/\omega = 0$ , and 0.48 ( $(f/\omega)^2 < 0.25$ ) and never saturates for  $f/\omega = 0.59$  ( $(f/\omega)^2 \geq 0.25$ ), as reported in Singh & Pal (2022). We refer each case with a unique name for example F075f/ω48, which indicates that  $F = 0.75$  and  $f/\omega = 0.48$ .

## 3. Results

We briefly explain the stability diagrams obtained by solving the linearized governing equations (Mathieu equations). Singh & Pal (2022) presents the details of the derivation of the linearized equations and their solution strategy. Figure 1 shows the stability diagrams at forcing amplitudes  $F = 1$  and 3. In figure 1a, the horizontal green line segment represents

$F$	$\omega$ (rad s <sup>-1</sup> )	$f/\omega$ ( $\eta_{cu} \approx$ )	$f/\omega$ ( $\eta_{cu} \approx$ )	$f/\omega$ ( $\eta_{cu} \approx$ )
0.75	0.67	0 ( $\approx 0.52$ )	0.48 ( $\approx 0.42$ )	0.59 (never saturate)
1	0.7	0 ( $\approx 0.44$ )	0.48 ( $\approx 0.40$ )	0.59 (never saturate)
2	0.8	0 ( $\approx 0.41$ )	0.48 ( $\approx 0.38$ )	0.59 (never saturate)
3	0.9	0 ( $\approx 0.355$ )	0.48 ( $\approx 0.34$ )	0.59 (never saturate)

Table 1: Simulation parameters. For all cases we use Atwood number  $\mathcal{A} = 0.01$ , initial mixing zone width  $L_0 = 0.096$  m, kinematic viscosity  $\nu = 1 \times 10^{-4}$  m<sup>2</sup> s<sup>-1</sup>, diffusion coefficient  $\kappa = 1 \times 10^{-4}$  m<sup>2</sup> s<sup>-1</sup>, and  $g_0 = 10$  m s<sup>-2</sup> (Briard *et al.* 2019; Singh & Pal 2022). Domain size:  $l_{x_1} = l_{x_2} = 2\pi$  m, and  $l_{x_3} = 2H = 3.5\pi$  m. Grid points:  $N_{x_1} = N_{x_2} = 512$  (uniform), and  $N_{x_3} = 512$  (non-uniform with clustering at the centre region of thickness  $1.53\pi$  m with  $\Delta x_{3min} = \Delta x_1 = \Delta x_2$ ).

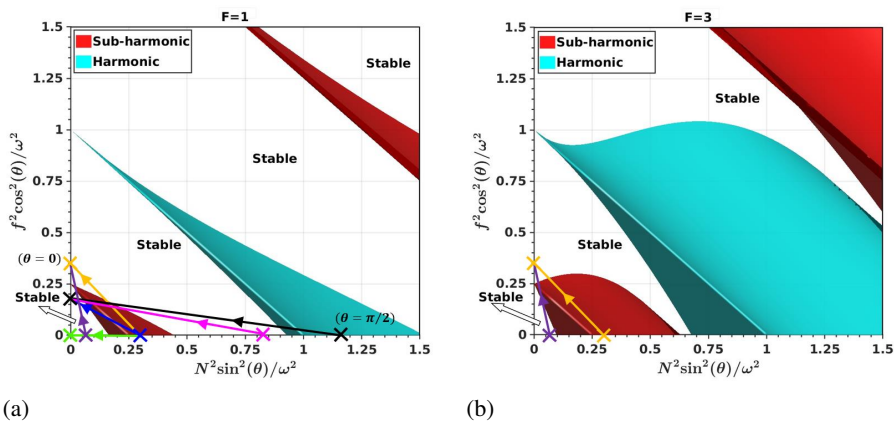


Figure 1: Top views of the three-dimensional Mathieu stability diagram (Singh & Pal 2022) at forcing amplitudes (a)  $F = 1$  and (b)  $F = 3$ . The stable (white) regions are in between the unstable red (sub-harmonic) and cyan (harmonic) colored tongues. The horizontal green line segment denotes the case without rotation ( $f = 0$ ) whereas rotation cases ( $f \neq 0$ ) are indicated by the inclined blue, pink, black, purple and orange line segments.

the case without rotation  $(f/\omega)^2 = 0$ . The inclined blue, pink and black line segments represent the cases with  $0 < (f/\omega)^2 < 0.25$  whereas the purple and orange line segments denote the cases with  $(f/\omega)^2 \geq 0.25$ . The right end of each segment ( $\times$ ; at  $\theta = \pi/2$ ) corresponds to the mixing zone size- $L$  ( $N^2/\omega^2 = 2\mathcal{A}g_0/(L\omega^2)$ ), while the left end ( $\times$ ; at  $\theta = 0$ ) corresponds to the Coriolis frequency  $f$ . When unstable  $\theta$ -modes in the sub-harmonic or harmonic tongues are excited by the periodic vertical forcing,  $L$  grows, and  $N^2/\omega^2$  moves toward the left. The  $\theta$ -modes are excited along the black line segment for  $F = 1$  as shown in figure 1a.  $L$  grows when the unstable  $\theta$ -modes along this line are excited. With time evolution, the right end of this inclined black line segment moves in the stable region between the leftmost sub-harmonic and harmonic tongues, as demonstrated by the pink  $\times$ . The process repeats, and  $N^2/\omega^2$  moves into the leftmost sub-harmonic regime represented by the blue  $\times$ . The sub-harmonic instabilities are triggered in this regime resulting in turbulent mixing. In contrast to the horizontal green line segment, more unstable  $\theta$ -modes are excited along the inclined blue line segment resulting in the triggering of more instabilities and an increase in turbulent kinetic energy (*t.k.e.*) for cases with  $0 < (f/\omega)^2 < 0.25$  as compared

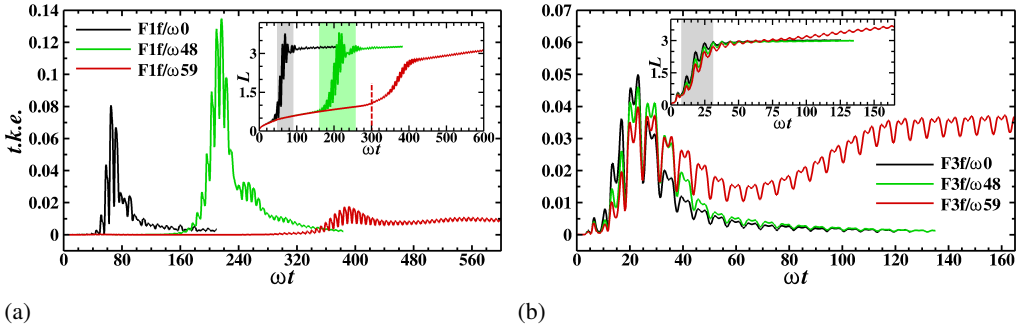


Figure 2: Evolution of vertically ( $x_3$ ) integrated  $t.k.e.$  for both without ( $f/\omega = 0$ ) and with ( $f/\omega = 0.48, 0.59$ ) rotation cases at (a)  $F = 1$ , and (b)  $F = 3$ . Inset shows the evolution of mixing zone size- $L$  with shaded regions indicating the sub-harmonic instability phase.

to the case without rotation. The instability finally saturates for  $(f/\omega)^2 < 0.25$  when no more unstable  $\theta$ -modes are excited, and the right end of the segment crosses the left boundary of the first sub-harmonic tongue and enters the leftmost stable region. For  $(f/\omega)^2 \geq 0.25$ , the orange line segment indicates that both unstable and stable  $\theta$ -modes are excited during the periodic vertical oscillations. The stable  $\theta$ -modes do not contribute to the triggering of instabilities, and therefore, we can deduce that higher rotation rates suppress turbulence. With an increase in  $F$ , the first sub-harmonic and harmonic tongues become wider, and the stable region between these tongues shrinks (figure 1b) resulting in the early onset of the sub-harmonic instability and turbulent mixing similar to the non-rotating case. An interesting feature for  $(f/\omega)^2 \geq 0.25$  is observed when  $N^2/\omega^2$  moves into the leftmost stable regime denoted by the purple  $\times$  in figures 1a and 1b. The purple line segment must always pass through the first sub-harmonic tongue. Therefore, the instability will never saturate, resulting in the sustenance of turbulence.

The evolution of vertically ( $x_3$ ) integrated turbulent kinetic energy  $t.k.e.$  ( $(\langle u_1^2 \rangle + \langle u_2^2 \rangle + \langle u_3^2 \rangle)/2$ , where  $\mathbf{u} = \mathbf{U} - \langle \mathbf{U} \rangle$ ), for  $F = 1$  is illustrated in figure 2a. The  $t.k.e.$  rapidly grows for  $F1f/\omega 0$  and  $F1f/\omega 48$  during the onset of the sub-harmonic instability. Eventually, the  $t.k.e.$  decays owing to the instability saturation. The  $t.k.e.$  for  $F1f/\omega 48$  is higher than  $F1f/\omega 0$  due to the excitation of more unstable  $\theta$ -modes in the sub-harmonic region, as discussed earlier. The  $t.k.e.$  decreases significantly for  $f/\omega = 0.59$  owing to the suppression of turbulence with increased rotation rate. Although small, the  $t.k.e.$  for  $F1f/\omega 59$  sustains owing to the continued triggering of the sub-harmonic instability, resulting in continuous turbulent mixing. A similar evolution of  $t.k.e.$  is observed for  $F = 0.75$ . At a higher forcing amplitude of  $F = 3$ , the magnitude of  $t.k.e.$  is similar for all  $f/\omega$  cases (figure 2b), indicating that the stabilizing effect of rotation is mitigated by the strong vertical forcing. Notice that the maximum value of  $t.k.e.$  for  $F1f/\omega 48$  is higher than  $F3f/\omega 48$ . This observation is also true for the non-rotating cases at respective forcing amplitudes. The longer sub-harmonic instability phase for  $F1f/\omega 48$  is the reason for a higher value of  $t.k.e.$  at  $F1f/\omega 48$  than at  $F3f/\omega 48$ . The sub-harmonic instability phase is the time interval between the onset and the saturation of the sub-harmonic instability and is demonstrated using the shaded regions in the evolution of the mixing zone size  $L$  in the inset. A long sub-harmonic instability phase for  $F = 0.75, 1$  signifies a delay in the saturation of the instabilities triggered during the low amplitude oscillations. Therefore, the instabilities get sufficient time to evolve and break into turbulence. In contrast to  $F = 0.75, 1$ , at  $F = 2, 3$ , the sub-harmonic instability phase is short. The instabilities saturate quickly and therefore do not have enough time to evolve and intensify turbulence. Interestingly, both  $F2f/\omega 59$  (figure not shown) and  $F3f/\omega 59$  manifest a

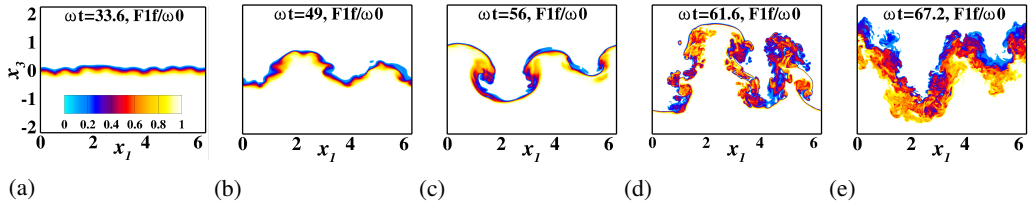


Figure 3: Contours of concentration field in vertical  $x_1 - x_3$  center plane ( $x_2 = \pi$ ) for case  $F1f/\omega 0$  at time instants (a)  $\omega t = 33.6$ , (b)  $\omega t = 49$ , (c)  $\omega t = 56$ , (d)  $\omega t = 61.6$ , and (e)  $\omega t = 67.2$ . Pure fluids of  $C = 1$  (denser) and  $C = 0$  (lighter) are made transparent.

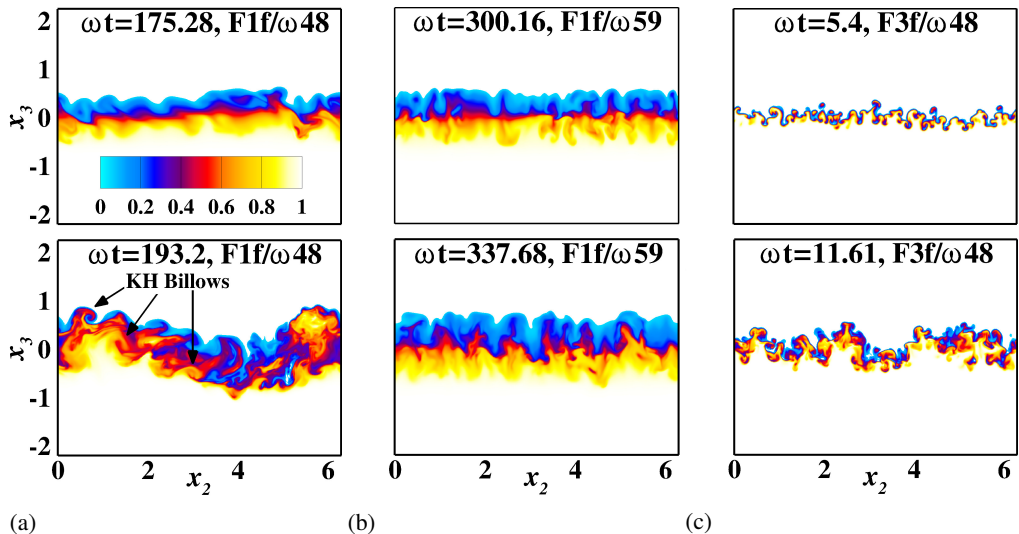


Figure 4: Contours of concentration field in vertical  $x_2 - x_3$  center plane ( $x_1 = \pi$ ) for rotation cases (a)  $F1f/\omega 48$ , (b)  $F1f/\omega 59$ , and (c)  $F3f/\omega 48$  at different time instants.

recovery in *t.k.e.* owing to the continuous triggering of the sub-harmonic instabilities.

The transition to turbulence phenomenon for the cases without and with rotation is analyzed using the contour plots of the concentration fields in a vertical plane. Figure 3 depicts the evolution of the interface of the concentration field for  $F1f/\omega 0$ . The initially perturbed interface, subjected to vertical and periodic accelerations, deforms into a wavy form owing to harmonic and sub-harmonic resonance as shown in figure 3a at  $\omega t = 33.6$ . This diffused wavy interface is amplified by the sub-harmonic instability, leading to the formation of mushroom-shaped waves as shown in figure 3b at  $\omega t = 49$ . In this instance, some waves with shorter wavelengths become disorganized and interact with each other, resulting in small velocity fluctuations. In the next oscillation, the amplitude of a longer wavelength wave amplifies, leading to the birth of a well-defined mushroom-shaped wave that bursts at the nodes as depicted in figure 3c at  $\omega t = 56$ . This process is known as wave-breaking of the Faraday waves (Cavelier *et al.* 2022) and is responsible for the onset of irreversible mixing. In the successive oscillations, the entire interface breaks down into small-scale structures leading to a full transition to turbulence as manifested in figures 3d and 3e. A similar dynamics is observed for  $F = 0.75$  and  $f/\omega = 0$  (see Movie 1 and Movie 4).

The combined effect of vertical oscillation and rotation in  $F1f/\omega 48$  results in roll-ups at multiple locations on the diffuse interface as shown in figure 4a at  $\omega t = 175.28$ . In subsequent oscillations, roll-ups will continue to form with a large size but in the opposite direction of the

previous one. These roll-ups will finally take the form of Kelvin-Helmholtz (KH) billows that will break into turbulence (see figure 4a at  $\omega t = 193.2$ ). Notice that the entire interface layer breaks into small structures in one oscillation resulting in a larger thickness of the turbulent mixing region as compared to  $F1f/\omega 0$  where the mushroom-shaped wave first breaks at the nodes and then turbulence spreads to the entire interface layer in the subsequent oscillations. Movie 2 included as the supplementary data demonstrates this event. This phenomenon is also responsible for larger *t.k.e.* in  $F1f/\omega 48$  as compared to  $F1f/\omega 0$  (figure 2a). We observe similar dynamics for  $F075f/\omega 48$  (see Movie 5). This phenomenon results in a gradual increase of irreversible mixing. When the Coriolis frequency increase to  $f/\omega = 0.59$  (case  $F1f/\omega 59$ ), we found that the effect of rotation is strong enough to suppress the formation of large amplitude waves and KH billows. Therefore, the turbulent mixing is only caused by the finger-shaped instability as depicted in figure 4b (see supplementary Movie 3 and Movie 6).

At higher forcing amplitude  $F = 3$  for  $f/\omega = 0.48$ , we observe the development of random finger-shaped structures on the interface that break in the first oscillation as shown in the figure 4c. Therefore, the turbulent mixing starts from the beginning of the periodic forcing. Additionally, the intensity of turbulence is low because of the shorter sub-harmonic instability phase at higher  $F$ . As the stabilizing effect of rotation is subdued at higher forcing amplitudes (Singh & Pal 2022), the turbulent mixing occurs by this mechanism for all  $f/\omega$  at  $F = 2, 3$  (figures not shown). We have included the animation of the concentration field for  $F3f/\omega 48$  as supplementary data (Movie 7).

Since there is no mean velocity field involved, we start the analysis of the irreversible mixing using the *t.k.e.* evolution equation as follows:

$$\frac{dt.k.e.}{dt} = \mathcal{P} - S - B - \epsilon - \frac{\partial \mathcal{T}_j}{\partial x_j}. \quad (3.1)$$

The turbulent production term  $\mathcal{P} = -\langle u_i u_j \rangle \frac{\partial \langle U_i \rangle}{\partial x_j}$  and the transport term  $\partial \mathcal{T}_j / \partial x_j$ , where  $\mathcal{T}_j = \langle p u_j \rangle - 2\nu \langle s_{ij} u_i \rangle + \frac{1}{2} \langle u_i u_i u_j \rangle$  are negligible. The energy input from the periodic forcing is  $S = 2\mathcal{A}g_0 F \cos(\omega t) \langle u_3 c \rangle$ . The buoyancy flux  $B = 2\mathcal{A}g_0 \langle u_3 c \rangle$  accounts for the reversible rate of exchange between *t.k.e.* and the total potential energy. The viscous dissipation  $\epsilon = 2\nu \langle s_{ij} s_{ij} \rangle$ , where  $s_{ij} = (\partial u_i / \partial x_j + \partial u_j / \partial x_i) / 2$ , acts as a sink for *t.k.e.*. We obtain an excellent closure of equation 3.1 for all the simulations signifying sufficient grid spacing in all directions to resolve all length scales.

The irreversible mixing is characterized by partitioning the total potential energy (TPE)  $E_{TPE} = 2\mathcal{A}g_0 \int_V C(\mathbf{x}) x_3 dV$  into the sum of an available potential energy (APE)  $E_{APE}$  and background potential energy (BPE)  $E_{BPE}$  (Winters *et al.* 1995). The BPE is the minimum potential energy a flow can have and is unavailable for extraction from the potential energy reservoir for driving macroscopic fluid motion. To estimate BPE of the flow at any instance of time, a volume element  $dV$  with concentration  $C$  at height  $x_3$  is adiabatically relocated to  $x_3^*$  such that the redistributed concentration field is statistically stable ( $dC(x_3^*)/dx_3^* \leq 0$ ) everywhere. We compute  $E_{BPE} = 2\mathcal{A}g_0 \int_V C(x_3^*) x_3^* dV$  and subtract it from  $E_{TPE}$  to obtain  $E_{APE}$  (Winters & Barkan 2013; Chalamalla & Sarkar 2015). Since our domain is closed by the top and bottom boundaries, the surface fluxes are zero. We derive the simplified equations for the evolution of TPE, BPE, and APE following Winters *et al.* (1995),

$$\frac{dE_{TPE}}{dt} = B_V + \phi_i, \quad (3.2a)$$

$$\frac{dE_{BPE}}{dt} = \phi_d, \quad (3.2b)$$

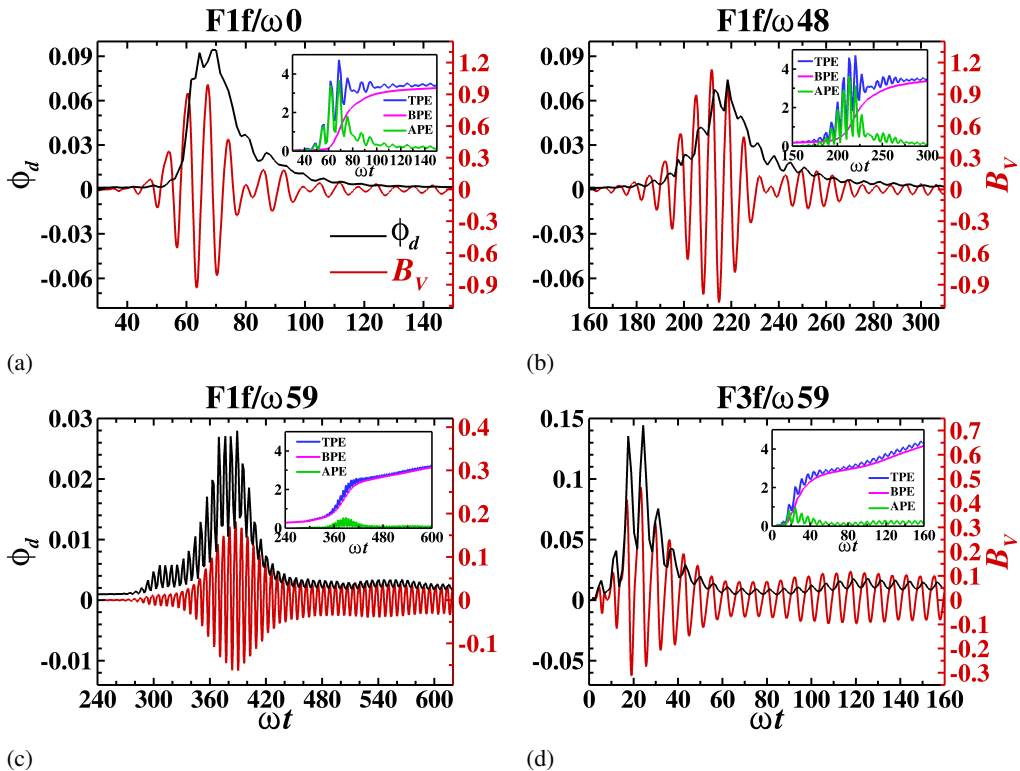


Figure 5: Time evolution of buoyancy flux ( $B_V$ ) and diapycnal flux ( $\phi_d$ ) at  $F = 1$  for (a)  $f/\omega = 0$ , (b)  $f/\omega = 0.48$ , (c)  $f/\omega = 0.59$ , and at  $F = 3$  for (d)  $f/\omega = 0.59$ . Insets: correspond to the evolution of TPE, BPE, and APE.

$$\frac{dE_{APE}}{dt} = B_V - (\phi_d - \phi_i). \quad (3.2c)$$

Here  $B_V$ ,  $\phi_i$ , and  $\phi_d$  are integrated over the volume  $V = l_{x_1}l_{x_2}H_s$ , and  $H_s$  is the vertical height of the domain excluding top and bottom sponge layer thickness. The  $B_V = \int B l_{x_1}l_{x_2}dx_3$  is volume integrated buoyancy flux and  $\phi_i = -2\mathcal{A}g_0\kappa A (\langle C_{top} \rangle - \langle C_{bot} \rangle)$ , where  $A = l_{x_1}l_{x_2}$ , the irreversible rate of conversion of internal to potential energy.  $\phi_d = 2\mathcal{A}g_0\kappa \int_V -\frac{dx_3^*}{dC} |\nabla C|^2 dV$  represents the rate of change of BPE due to irreversible diapycnal flux and is a measure of the irreversible mixing. Notice that as  $\phi_d \geq 0$ , it always acts as a sink of APE, increasing  $E_{BPE}$ . Since we have periodic forcing in the domain, we choose to calculate the cumulative mixing efficiency (Peltier & Caulfield 2003; Briard *et al.* 2019) as follows:

$$\eta_{cu}(t) = \frac{\int_{t_1}^{t_2} \phi_d dt}{\int_{t_1}^{t_2} (\phi_d + \epsilon_V) dt}. \quad (3.3)$$

Here  $\epsilon_V = \int \epsilon l_{x_1}l_{x_2}dx_3$  is the volume integrated viscous dissipation. The cumulative mixing efficiency  $\eta_{cu}$  measures the irreversible loss of initially available energy that expends in irreversible mixing in contrast to the total energy loss to the irreversible mixing and viscous dissipation.

Figure 5 illustrates the temporal evolution of the reversible buoyancy flux  $B_V$  and the diapycnal flux  $\phi_d$ . We also include the evolution of TPE, APE, and BPE in the inset of each

figure. The *t.k.e.* for  $F1f/\omega 0$  increases due to the onset of sub-harmonic instabilities and the formation and breaking of mushroom-shaped waves. This increased *t.k.e.* results in an increase in  $B_V$ , and therefore, TPE also increases as demonstrated in figure 5a. A fraction of this TPE is APE. Some part of this APE can convert back to *t.k.e.* via  $B_V$  and the rest can convert to internal energy that increases BPE owing to  $\phi_i$ . Since  $B_V$  increases, APE also increases at  $\omega t \approx 46 - 55$ . The remaining portion of TPE goes to BPE via  $\phi_d$ . The  $\phi_d$  also starts increasing after  $\omega t \approx 55$ . After wave-breaking, the entire interface layer breaks, resulting in a rapid increase of  $\phi_d$  signifying rapid conversion of TPE into BPE. When the instabilities saturate at  $\omega t \approx 70$ , *t.k.e.*,  $B_V$  and APE decrease, and TPE saturates. The BPE also saturates, as demonstrated by a decreasing  $\phi_d$ . Similar to  $F1f/\omega 0$ , we observe that  $B_V$  for  $F1f/\omega 48$  increases at  $\omega t \approx 180$  owing to an increase in *t.k.e.* (see figure 5b). At the same instance,  $B_V$ , TPE, and APE also increase. We find a gradual increase of  $\phi_d$  and BPE for  $F1f/\omega 48$  compared to a rapid increase for  $F1f/\omega 0$ . The reason is the continuous formation and breaking of the KH billows at the diffuse interface during the sub-harmonic instability phase for  $F1f/\omega 48$ . With the saturation of the instability,  $B_V$  and APE start decreasing, resulting in the increase and eventual saturation of BPE as illustrated by the gradual decrease of  $\phi_d$  to zero in figure 5b. This gradual decrease in  $\phi_d$  denotes that irreversible mixing is sustained for an extended period than  $F1f/\omega 0$ , owing to the long sub-harmonic instability phase. For  $F1f/\omega 59$ , there is a significant delay in the onset of sub-harmonic instability. Therefore,  $B_V$  and APE  $\sim 0$  till  $\omega t \approx 280$ . During this period, the initial concentration profile diffuses (Winters *et al.* 1995), increasing the TPE at the rate  $\phi_i$ . Therefore, the potential energy increases at the expense of the internal energy of the fluid. Since APE remains close to zero,  $TPE \approx BPE$ , and  $\phi_d(0.001) \approx \phi_i(0.0008)$  from equation 3.2c till  $\omega t \approx 280$ . This is demonstrated in figure 5c. Notice that higher rotation rate suppresses turbulence (see Movie 3), resulting in smaller *t.k.e.* and  $B_V$  (figure 5c) compared to the previous cases.  $B_V$  increases after  $\omega t \approx 280$ , increasing TPE. However, smaller  $B_V$  signifies that only a minor portion of the TPE is available for conversion to *t.k.e.* as shown by small APE in the inset of figure 5c. The bulk of TPE goes in BPE, and the evolution of  $\phi_d$  shows its rate of increase. The instability never saturates for  $F1f/\omega 59$  and triggers continuously, resulting in the sustenance of *t.k.e.* and  $B_V$ . The TPE also continues to increase due to  $B_V$ , and APE continues to remain small. The  $\phi_d$  oscillates and remains greater than zero indicating a continuous increase in BPE with time and signifying the sustenance of irreversible mixing for higher rotation rates. For  $F = 2, 3$  and  $f/\omega = 0, 0.48$  the *t.k.e.*,  $B_V$ , TPE, and APE increase from the beginning of the periodic forcing (figure not shown). Subsequently, BPE and  $\phi_d$  also increase. Since the instabilities saturate quickly for these cases,  $B_V$  and APE become  $\sim$  zero. The BPE saturates, and the  $\phi_d$  also tends to zero, signifying the ceasing of irreversible mixing. The initial evolution of energetics for  $F = 2, 3$  for  $f/\omega = 0.59$  (figure 5d for  $F3f/\omega 59$ ) is similar to the cases discussed above. However, at a later stage, the evolution resembles the case  $F1f/\omega 59$  and demonstrates non-zero  $B_V$  and  $\phi_d$ , signifying a continuous increase in BPE and sustenance of irreversible mixing. We summarize the energy pathways in figure 6a.

The time evolution of  $\eta_{cu}$  is plotted in the figure 6b. For  $F075f/\omega 0$  case,  $\eta_{cu}$  decreases rapidly when the diapycnal flux  $\phi_d$  and viscous dissipation  $\epsilon_V$  increases. It attains a minimum value of  $\sim 0.52$  after instability saturation. We find that in the presence of rotation for  $F075f/\omega 48$ , the  $\eta_{cu}$  reduces to  $\sim 0.42$ , which implies that the mixing is not as efficient as for  $F075f/\omega 0$ . For  $F075f/\omega 59$ , the  $\eta_{cu}$  decreases continuously owing to the continuous irreversible mixing. However, the mixing is still more efficient ( $\eta_{cu} \approx 0.57$  at  $\omega t \approx 950$ ) than  $F075f/\omega 0$  and  $F075f/\omega 48$ . For  $F1f/\omega 0$ ,  $\eta_{cu}$  is  $\sim 0.44$  similar to that obtained by Briard *et al.* (2019). At  $F = 1$  and  $f/\omega = 0.48$   $\eta_{cu} \sim 0.4$  whereas for  $f/\omega = 0.59$  the cumulative mixing efficiency is 0.433 at  $\omega t = 600$ , but keeps decreasing with time. We find that the mixing becomes less

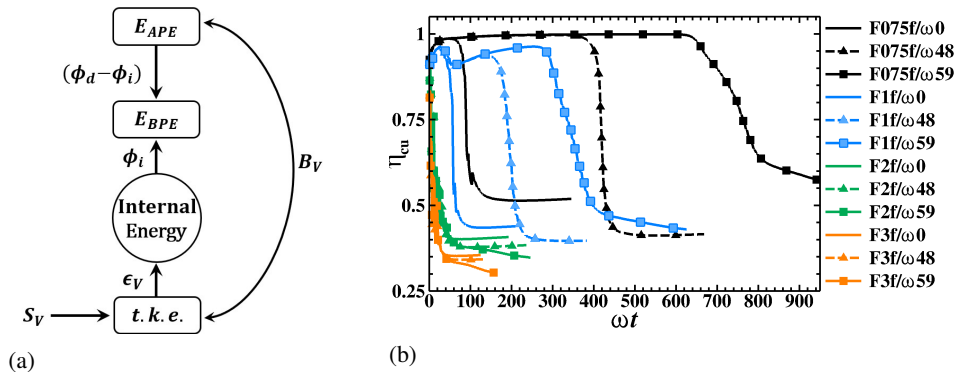


Figure 6: (a) Schematic of energy pathways,  $S_V$  is the volume integrated  $S$ . (b) time evolution of cumulative mixing efficiency  $\eta_{cu}$ ; at forcing amplitudes  $F = 0.75, 1, 2,$  and  $3$  for each without rotation ( $f/\omega = 0$ ) and with rotation ( $f/\omega = 0.48, 0.59$ ) cases.

efficient with an increase in  $F$  for all  $f/\omega$  values, and the mixing efficiency continues to decrease for the  $f/\omega = 0.59$  cases.

#### 4. Conclusions

We perform DNS to investigate the effect of rotation on the turbulent mixing driven by Faraday instability in two miscible fluids subjected to vertical oscillations. At lower forcing amplitudes  $F = 0.75$  and  $1$ , the  $t.k.e.$  increases with an increase in the Coriolis frequency from  $f/\omega = 0$  to  $0.48$ . This enhancement is due to the excitement of more unstable  $\theta$ -modes in the sub-harmonic region resulting in the continuous development and breaking of KH billows at the interface layer during the sub-harmonic instability phase. The mechanism of turbulence generation for the cases without rotation is different. A well-defined mushroom-shaped wave evolves for  $f/\omega = 0$  cases that disintegrate at the nodes. Subsequently, the turbulence spreads to the entire mixing layer in successive oscillations. In contrast to  $f/\omega = 0, 0.48$ ,  $f/\omega = 0.59$  significantly suppresses turbulence owing to the development and gradual breaking of finger-shaped structures. At higher forcing amplitudes  $F = 2$  and  $3$  for  $f/\omega = 0, 0.48$ , and  $0.59$ , we observed the breakdown of finger-shaped structures in the first two oscillations of periodic forcing resulting in the early onset of turbulence. However, the turbulence is less intense and short-lived than at lower forcing amplitudes owing to the shorter sub-harmonic instability phase. An interesting finding is an increase in  $t.k.e.$  after an initial decrease for  $f/\omega = 0.59$  due to the continuous triggering of the sub-harmonic instabilities.

We also analyze the energetics associated with the flow. An increase in  $t.k.e.$  for the cases with  $f/\omega = 0.48$  at  $F = 0.75, 1$  implies an increase in the buoyancy flux and therefore, TPE also increases. A portion of this TPE is APE. Some part of this APE converts back to  $t.k.e.$  via the buoyancy flux, whereas the rest is converted to internal energy, increasing the BPE through  $\phi_i$ . The rest of the TPE goes to BPE through  $\phi_d$  resulting in irreversible mixing. When the  $t.k.e.$  starts decreasing due to instability saturation,  $B_V$  also decreases, signifying a decrease in APE. Therefore, BPE saturates, and  $\phi_d$  approaches zero. Interesting, for  $f/\omega = 0.48$  the irreversible mixing sustains for a longer period than  $f/\omega = 0$  due to a longer sub-harmonic instability phase. The cases with a higher rotation rate of  $f/\omega = 0.59$  demonstrate a significant delay in the onset of sub-harmonic instability, owing to which  $B_V$  and APE remain zero. The initial concentration profile diffuses during this period to increase TPE at the rate  $\phi_i$ . This TPE goes completely to BPE at the same rate since

$\phi_d$  becomes equal to  $\phi_i$  according to equation 3.2c. After the onset of the sub-harmonic instability, the *t.k.e.*,  $B_V$ , and APE increase. However, these values remain significantly smaller than  $f/\omega = 0, 0.48$  cases. The TPE also increases due to  $B_V$ . Since APE is small, the bulk of the portion of TPE expends to BPE via  $\phi_d$ . Since the instabilities never saturate for  $f/\omega = 0.59$ , the *t.k.e.*,  $B_V$  and APE although small remains non-zero. Therefore, TPE increases continuously and expends to BPE via  $\phi_d$ . The  $\phi_d$  remains greater than zero, signifying a continuous increase in BPE and irreversible mixing. At  $F = 2, 3$ ,  $\phi_d$  increases from the beginning of the vertical forcing for all  $f/\omega$  cases. However, the irreversible mixing for  $f/\omega = 0, 0.48$  does not sustain for long owing to the quick saturation of the sub-harmonic instability. Since the instability never saturates for  $f/\omega = 0.59$ ,  $\phi_d$  demonstrates continuous oscillations and therefore, continuous mixing. Finally, the mixing phenomenon is quantified using cumulative mixing efficiency. We conclude that for rotation rates  $f^2/\omega^2 > 0.25$  and at lower forcing amplitudes  $F = 0.75, 1$  the mixing process is more efficient.

**Supplementary data.** Supplementary movies are available at [https://doi.org/\\*\\*.\\*\\*\\*\\*/jfm.\\*\\*\\*...](https://doi.org/**.****/jfm.***...)

**Acknowledgements.** We gratefully acknowledge Dr. Vamsi K. Challamalla for providing us the computer program for the calculation of TPE,  $x_3^*$ , BPE and  $\phi_d$ .

## REFERENCES

- AMIROUDINE, SAKIR, ZOUESHTIAGH, FARZAM & NARAYANAN, RANGA 2012 Mixing generated by faraday instability between miscible liquids. *Physical review E* **85** (1), 016326.
- ANDREWS, MALCOLM J & SPALDING, DUDLEY BRIAN 1990 A simple experiment to investigate two-dimensional mixing by rayleigh–taylor instability. *Physics of Fluids A: Fluid Dynamics* **2** (6), 922–927.
- BRIARD, ANTOINE, GOSTIAUX, LOUIS & GRÉA, BENOÎT-JOSEPH 2020 The turbulent faraday instability in miscible fluids. *Journal of Fluid Mechanics* **883**.
- BRIARD, ANTOINE, GRÉA, BENOÎT-JOSEPH & GOSTIAUX, LOUIS 2019 Harmonic to subharmonic transition of the faraday instability in miscible fluids. *Physical Review Fluids* **4** (4), 044502.
- CAVELIER, M, GRÉA, B-J, BRIARD, A & GOSTIAUX, L 2022 The subcritical transition to turbulence of faraday waves in miscible fluids. *Journal of Fluid Mechanics* **934**.
- CHALAMALLA, VAMSI K & SARKAR, SUTANU 2015 Mixing, dissipation rate, and their overturn-based estimates in a near-bottom turbulent flow driven by internal tides. *Journal of Physical Oceanography* **45** (8), 1969–1987.
- DIWAKAR, SV, ZOUESHTIAGH, FARZAM, AMIROUDINE, SAKIR & NARAYANAN, RANGA 2015 The faraday instability in miscible fluid systems. *Physics of Fluids* **27** (8), 084111.
- FARADAY, MICHAEL 1831 Xvii. on a peculiar class of acoustical figures; and on certain forms assumed by groups of particles upon vibrating elastic surfaces. *Philosophical transactions of the Royal Society of London* (121), 299–340.
- GRÉA, B-J & ADOU, A EBO 2018 What is the final size of turbulent mixing zones driven by the faraday instability? *Journal of Fluid Mechanics* **837**, 293–319.
- PELTIER, WR & CAULFIELD, CP 2003 Mixing efficiency in stratified shear flows. *Annual review of fluid mechanics* **35** (1), 135–167.
- SINGH, NARINDER & PAL, ANIKESH 2022 The onset and saturation of the faraday instability in miscible fluids in a rotating environment. *arXiv preprint arXiv:2207.13739*.
- WINTERS, KRAIG B & BARKAN, ROY 2013 Available potential energy density for boussinesq fluid flow. *Journal of Fluid Mechanics* **714**, 476–488.
- WINTERS, KRAIG B, LOMBARD, PETER N, RILEY, JAMES J & D’ASARO, ERIC A 1995 Available potential energy and mixing in density-stratified fluids. *Journal of Fluid Mechanics* **289**, 115–128.
- ZOUESHTIAGH, F, AMIROUDINE, S & NARAYANAN, R 2009 Experimental and numerical study of miscible faraday instability. *Journal of fluid mechanics* **628**, 43–55.